JGR Planets

RESEARCH ARTICLE
10.1029/2022JE007196

Spatio-Temporal Level Variations of the Martian Seasonal South Polar Cap From Co-Registration of MOLA Profiles

Haifeng Xiao[1], Alexander Stark[2], Frédéric Schmidt[3,4], Jingyan Hao[5], Shu Su[1], Gregor Steinbrügge[6], and Jürgen Oberst[1]

[1]Institute of Geodesy and Geoinformation Science, Technische Universität Berlin, Berlin, Germany, [2]Institute of Planetary Research, German Aerospace Center (DLR), Berlin, Germany, [3]CNRS, GEOPS, Université Paris-Saclay, Orsay, France, [4]Institut Universitaire de France (IUF), Paris, France, [5]Division of Space Technology, Kiruna Space Campus, Luleå University of Technology, Luleå, Sweden, [6]Department of Geophysics, Stanford University, Stanford, CA, USA

Key Points:

- Using co-registration of Mars Orbiter Laser Altimeter profiles, spatio-temporal level variations of the seasonal snow/ice deposits at the Martian south pole are obtained
- Maximum level can be up to 2.5 m; Peak level increased by ∼0.5 m at the Residual South Polar Cap from Martian Year 24 (MY24) to MY25
- Obtained bulk density map of the seasonal deposits implies that snowfall concentrates at the Residual South Polar Cap and its surroundings

Supporting Information:

Supporting Information may be found in the online version of this article.

Correspondence to:

H. Xiao,
Haifeng.Xiao@campus.tu-berlin.de

Citation:

Xiao, H., Stark, A., Schmidt, F., Hao, J., Su, S., Steinbrügge, G., & Oberst, J. (2022). Spatio-temporal level variations of the Martian Seasonal South Polar Cap from co-registration of MOLA profiles. *Journal of Geophysical Research: Planets*, *127*, e2022JE007196. https://doi.org/10.1029/2022JE007196

Received 17 JAN 2022
Accepted 27 JUN 2022

Abstract The seasonal deposition and sublimation of CO_2 represents a major element in the Martian volatile cycle. Here, co-registration strategies are applied to Mars Orbiter Laser Altimeter profiles to obtain spatio-temporal variations in snow/ice level of the Seasonal South Polar Cap (SSPC), in grid elements of 0.5° in latitude from 60° to 87°S and 10° in longitude. The maximum snow/ice level in the range of 2–2.5 m is observed over the Residual South Polar Cap. Peak level at the Residual South Polar Cap in Martian Year 25 (MY25) are found to be typically ∼0.5 m higher than those in MY24. The total volume is estimated to peak at approximately 9.4×10^{12} m^3. In addition, a map of average bulk density of the SSPC during its recession is derived. It implies much more snowfall-like precipitation at the Residual South Polar Cap and its surroundings than elsewhere on Mars.

Plain Language Summary Each Martian year, up to one third of the atmosphere's CO_2 is transported from pole to pole, being deposited and sublimated depending on the season. Accurate measurements of snow level and volume variations of the resulting seasonal polar caps can serve as crucial constraints on the Martian volatile cycles. In this study, we apply new approaches of analyzing the Mars Orbiter Laser Altimeter profiles, which lead to spatially and temporally resolved measurements of snow/ice level of the Seasonal South Polar Cap (SSPC). Based on that, the maximum snow level, interannual maximum level change from Martian Year 24 (MY24) to MY25, and how the volume of the SSPC changes with time are measured. We also estimate the bulk density of the snow/ice deposition during southern winter. It is inferred that there is much more snowfall at the Residual South Polar Cap and its surroundings than elsewhere on the planet.

1. Introduction

Each Martian year, approximately 30% of the atmosphere's CO_2 mass is in exchange with the polar surfaces through deposition/sublimation (Leighton & Murray, 1966). The seasonal CO_2 polar caps resulting from repeated depositions of snow/ice can extend down to 50°S/N (Piqueux et al., 2015). Temporal variations of the level and volume of snow/ice associated with the deposition/sublimation process can put crucial constraints on the Mars climate system and volatile circulation models. Additionally, this amount of snow and ice is significant enough to cause seasonal deflection of the lithosphere (Wagner et al., 2022). Constraining the level and mass of the seasonal portion of the polar cap is essential in properly modeling this deflection. Measurements of the level of snow/ice of the seasonal polar caps have been made by the Mars Orbiter Laser Altimeter (MOLA) onboard the Mars Global Surveyor (MGS, Smith et al., 2001; Aharonson et al., 2004; Smith & Zuber, 2018), measuring rock shadow lengths in high-resolution images to deduce the seasonal changes in rock heights on the surface (Mount & Titus, 2015), and precise radiative transfer models using imaging spectroscopy (Andrieu et al., 2018). Compared with the latter two that are spatially and temporally limited due to data availability, MOLA data cover the entire polar regions. Based on profile analysis at different latitudina annuli, Smith et al. (2001) measured the maximum seasonal level of snow/ice to be ∼1 m at both poles. In a different approach, Aharonson et al. (2004) fitted sinusoidal functions with annual and semi-annual terms to MOLA cross-over height residuals and estimated the maximum level to reach ∼1.5 m at the north pole and ∼2.5 m at the south pole.

The "cryptic region" at Martian south pole during the southern spring is roughly located from 50° to 210°E and poleward of 70°S (see also Figure 1 of Hansen et al. (2010)). It is so described as it possesses low temperatures

that indicate the presence of CO_2 ice, and at the same time low albedo, an indicator of dust. Kieffer (2007) suggested that the ability to maintain low temperatures in the presence of low albedo can be achieved in the presence of a translucent slab of ice. In this case, the sunlight penetrates through the translucent slab ice, heating the ground, triggering sublimation at the base of the slab ice, resulting in later CO_2 gas jetting and dust ejection. This cold-jetting is hypothesized to relocate more mass of dust than the dust storms or the cumulative effect of dust devils (Piqueux & Christensen, 2008). Thus, it is among one of the most active erosive processes on Mars which creates various geological features among which are the troughs in the polar surface known as "spiders" or araneiform terrain (e.g., Diniega et al., 2021; Hansen et al., 2010; Hao et al., 2019; Kieffer et al., 2006; Portyankina et al., 2017). A review of the observations of these exotic processes can be found in Schmidt and Portyankina (2018). The thickness of the Seasonal South Polar Cap (SSPC) is proposed to be a key factor in controlling the cold-jetting process (Hao et al., 2020). However, little work has been done so far to investigate the spatio-temporal variations of the snow/ice level of the SSPC, for example, in the cryptic and non-cryptic regions (Aharonson et al., 2004; Jian & Ip, 2009; Smith et al., 2001).

As the orbit of MGS does not feature repeat tracks that are specifically devoted to the detection of surface level variations, a common approach is to use differential height measurements where MOLA profiles intersect (Aharonson et al., 2004; Smith et al., 2001). The cross-over method can suffer from significant interpolation errors as the spacing between consecutive MOLA footprints is large (~300 m). Besides, shallow angles between intersecting profiles, especially at regions close to the equator, provide an unfavorable geometry for the estimation of cross-over height differences (Mazarico et al., 2010). Residual orbit, pointing, and timing errors can translate into lateral shifts of the MOLA profiles and further contaminate the results (see also Steinbrügge et al., 2015; Xiao, Stark, Steinbrügge, et al., 2021). In a previous effort (Xiao, Stark, Steinbrügge, et al., 2022), an alternative approach for analyzing laser altimetry data was proposed to study the dynamics of Mars' polar areas. In that study, we demonstrated that co-registering individual altimetric profiles obtained at different times to static digital terrain model (DTMs) of a given region allows meaningful detection of small elevation variations down to 5 cm. This precision is even higher than the MOLA inherent ranging resolution of 37.5 cm, which is achieved by involving large quantities of altimetric measurements in the co-registration. As part of that study, we devised a post-correction procedure based on pseudo cross-overs to remove temporal biases in MOLA footprint heights and other sources of residual errors. Providing that a DTM is available, any particular pair of laser profile segments will form a pseudo cross-over (Barker et al., 2016; Xiao, Stark, Steinbrügge, et al., 2022). The connection between the profiles is established by a reference DTM overlapping with both profiles. Hence, the height difference between those profiles that do not necessarily cross each other is assigned as the difference of their height corrections in their co-registrations to the reference DTM with parameterization in map coordinates, that is, line, sample, and height.

Once the level of the SSPC is derived, its bulk density can be calculated by combining them with the corresponding mass variation measurements. Similar magnitudes have been obtained for the total mass of the SSPC from various sources and techniques, for example, $\sim 6 \times 10^{15}$ kg from gravity variations (Karatekin et al., 2006), 6×10^{15} kg from the Gamma Ray Spectrometer (GRS; Kelly et al., 2006), $6.1 \pm 0.6 \times 10^{15}$ kg from the High Energy Neutron Detector (HEND; Litvak et al., 2007), and $5.6 \pm 1.3 \times 10^{15}$ kg from energy balance modeling (Schmidt et al., 2010). The bulk density estimates can be directly converted to porosity which can constrain depositional mechanisms (atmospheric precipitation as snowfall vs. direct surface condensation as frost) and the microphysical states of the seasonal CO_2 deposits (granular vs. slab ice). Unfortunately, available bulk density estimates are mainly represented as time-averages over extensive regions. Still, large discrepancies exist between these estimates, for example, 910 ± 230 kg/m^3 which represents as an upper limit from Smith et al. (2001), maximum density of ~1,200 kg/m^3 for the SSPC from Smith and Zuber (2018), and $400 - 1{,}250$ kg/m^3 for the SSPC at latitudes between 80° and 90°S from Litvak et al. (2007). However, snow/ice bulk density can spatially differ and continuously increase in time due to densification mechanisms such as annealing and re-crystallization (Matsuo & Heki, 2009).

In this study, we focus on south polar regions from 60° to 87°S. First, seasonal variations in level of snow/ice at grid elements of 0.5° in latitude and 10° in longitude are derived. Measurements at these individual grid elements are then subject to further examination. The bulk density of the SSPC at the recession phase is then obtained for each grid element by combining the level variation measurements and the mass change rates inverted from an

energy balance model (Schmidt et al., 2009, 2010). Temporal evolution of the bulk density of the SSPC during southern winter and spring is also derived and discussed.

2. Data

2.1. Reprocessed MOLA Data Set

MOLA mapped the topography of Mars within footprints of approximately 160 m in diameter with a center-to-center along-track spacing of around 300 m (Zuber et al., 1992). The MOLA Precision Experimental Data Record (PEDR) data set (Smith et al., 2003) features more than 8,700 profiles acquired in the mapping and extended phases of MGS from March 1999 to June 2001, which spans more than one full Martian year (MY24 to MY25). The PEDR data set was geolocated using a MGS trajectory and a Mars rotational model dating back to 2003. Therefore, we have incorporated an updated orbit model from Konopliv et al. (2006) and IAU2015 Mars rotational model as in Archinal et al. (2018) to update the MOLA geolocation (Xiao, Stark, Chen, & Oberst, 2022, Xiao, Stark, Steinbrügge, et al., 2022). The motion of the spacecraft during laser time-of-flight has been considered. Meanwhile, a pointing aberration, which the PEDR processing ignored, has been added during the reprocessing to account for the special relativity effects (Xiao, Stark, Steinbrügge, et al., 2021). The self-consistency of the reprocessed MOLA PEDR, evaluated as the root-mean-square (RMS) height discrepancy at cross-overs in equatorial and tropical regions without the seasonal CO_2 condensation/deposition, has been reduced from 8.2 to 7.0 m, a nearly 15% improvement (Xiao, Stark, Steinbrügge, et al., 2022).

2.2. Mass Change Rate Measurements

Cubes from OMEGA, that is, Observatoire pour la Minéralogie, l'Eau, les Glaces et l'Activité, the visible and infrared imaging spectrometer onboard the Mars Express (Bibring et al., 2004), are used to provide mass estimates of snow/ice. Using surface properties deduced from the OMEGA spectral cubes, Schmidt et al. (2009) proposed an energy balance model, and modeled the mass deposition/sublimation rates from 30° to 90°S with temporal resolution of 5° in solar longitude. Note that the actual albedo used in the radiative transfer model is valid only from L_s ~120° to ~300°. Thus, the mass change rates not falling within this period can be unrealistic. These data are used as they were from Schmidt et al. (2009, 2010) which are provided to us as grid maps with spatial resolution of 920 m in a south polar stereographic projection (available at Schmidt (2022)). To facilitate the comparison to the derived temporal level variations, the spatio-temporal maps of these mass change rates are resampled into grid elements of 0.5° in latitude and 10° in longitude.

3. Methods

We generate a reference DTM from 40° to 87°S from the self-registration of the reprocessed MOLA profiles (available at Xiao, Stark, Schmidt, et al. (2021)). Then, post-corrected spatio-temporal level variations of the SSPC (refer to Figure 5 in Xiao, Stark, Steinbrügge, et al. (2022) for a detailed schematic) and its mean bulk density during the recession phase are derived. These procedures are described in the following subsections.

3.1. Reference DTM From MOLA Self-Registration

As preparation, We build a reliable reference DTM for the area of interest at (40°, 87°S) to be used in the measurements of seasonal variations in surface elevation. We adopt self-registration of the reprocessed MOLA profiles (Stark et al., 2015; Xiao, Stark, Steinbrügge, et al., 2022). The self-registration is carried out through multiple iterations. For each iteration, a random subset (25%) of laser profiles is selected and then co-registered to an intermediate DTM constructed from the rest of profiles. The co-registration is parameterized in line, sample, and height in the polar stereographic projection centered at the south pole. This process is iterated 30 times until no outliers are seen by visual inspection and the MOLA reference DTM is made out of these self-consistent profiles. To minimize the interference of the spatially and temporally inhomogeneous level variations of the SSPC in the self-registration processes, we follow a divide-and-conquer strategy. First, we divide the region into five contiguous annuli, that is, (40°S, 50°S), (50°S, 60°S), (60°S, 69°S), (69°S, 78°S), and (78°S, 87°S), to which we apply the self-registration technique separately. We obtain five self-coherent DTMs with spatial resolutions of 1 km/pixel, which are mosaicked into one reference DTM, conveniently prepared in stereographic projection.

3.2. Seasonal Level Variation Measurements

The proposed method measures the CO_2 seasonal level variation by taking advantage of a local co-registration process (Xiao, Stark, Steinbrügge, et al., 2022). Measurements are made over a grid of elements 0.5° in latitude and 10° in longitude, from 60° to 87°S. First, a grid element, a laser track crossing the specific grid element, and one laser footprint along the track are chosen. Then, all footprints acquired within ±30 s of the acquisition time of the footprint in question are selected to form a local profile segment. For nadir-pointing profiles, the selected segment extends to about 90 km and contains about 600 footprints in total. Then, the selected profile segment is co-registered to the underlying reference DTM with parameterization in stereographic map coordinates (Xiao, Stark, Steinbrügge, et al., 2022). The height correction of the aforementioned co-registration process is considered as our observable. The above process is then repeated for all footprints along all profiles that fall within the grid element. Finally, all observables representing different acquisition times, are median-binned, with a temporal resolution of ∼5 days, to form a level variation time series. The precision of each median is represented by the scaled median absolute deviation (Leys et al., 2013).

3.3. Post-Correction Procedure

It is necessary to correct for a global systematic temporal bias in MOLA height measurements, which is mimicking a seasonal 2 m peak-to-peak amplitude elevation variation signal (Aharonson et al., 2004). This bias still remains after the reprocessing using updated auxiliary information (Xiao, Stark, Steinbrügge, et al., 2022). To correct for this artifact while aiming for high-precision temporal level variations, we employ a process known as regional pseudo cross-over adjustment (RPCA) which combines the concept of DTM-based pseudo cross-overs and the local co-registration technique (Xiao, Stark, Steinbrügge, et al., 2022). A pseudo cross-over is formed by two laser profile segments that do not necessarily intersect each other. The height difference at a pseudo cross-over is assigned as the difference in the height corrections when these two profile segments are aligned to the reference DTM using a co-registration in stereographic map coordinates. In the RPCA process, we try to minimize the height misfits at pseudo cross-overs acquired within 5 days and solve for height adjustments for each of the profiles. Ridge regression is adopted in the RPCAs to solve the ill-posed problem due to the correlation between the model parameters, that is, height adjustment for each of the profiles. The ridge trace approach is used to pin down the optimal regularization strength. Since the profile segments do not necessarily have to intersect, the available number of "cross-overs" is normally multiplied. By utilizing the co-registration in the pseudo cross-over formulation, the errors due to interpolation and lateral shifts of the profiles associated with the traditional cross-overs can be avoided and compensated, respectively. Furthermore, the profile segment pair forming a pseudo cross-over can be widely separated across the region, offering "global" constraints in the adjustment.

Specifically, we apply two consecutive RPCAs in a post-correction procedure as "bi-RPCA" to link the polar regions with CO_2 level variation signal and a tropical annulus without (Xiao, Stark, Steinbrügge, et al., 2022). Each of the profile segments falling within (44°S, 56°S) annulus is co-registered in stereographic map coordinates to the reference DTM to obtain height corrections per profile for the global systematic temporal bias. The first RPCA is then applied to acquire the adjustments for the aforementioned height corrections. Assuming that the systematic temporal bias is spatially invariable and equals the one acquired at (44°S, 56°S), these height corrections are then adjusted and applied to the profile segments within a polar grid element. Subsequently, the second RPCA is performed at that grid element to obtain the height corrections for each of the profiles due to all categories of residual errors, including that of the reprocessed MOLA profiles, the co-registration process, and the reference DTM. The local profile segments are formed by selecting footprints acquired within ±30 s of the central footprints along the profiles intercepted by the grid element. In order to involve more pseudo cross-overs in the second RPCA, grid elements within 80° to 87°S are extended by an extra of 5° in longitude on each side. Similarly, grid elements within 70° to 80°S and 60° to 70°S are extended an extra of 10° and 15°, respectively. Finally, height corrections from both of these RPCAs are applied to observables from Section 3.2, which are median-binned to form a seasonal level variation time series.

3.4. Gridded Products

Two essential characteristics, that is, maximum level of the SSPC and MY24 to MY25 peak level variation, are then extracted at individual grid elements and gridded as to be spatially examined over the south pole (available at Xiao, Stark, Schmidt, et al. (2021)).

3.5. Bulk Density Map of the Snow/Ice Deposition

Mass change rates from a energy balance model (Section 2.2) are used for estimation of the bulk densities of the SSPC within each of the grid elements. These mass change rates are integrated and examined against the obtained seasonal level variations to determine the average bulk density of the SSPC during recession phase. Then, the obtained bulk density estimates are gridded to be analyzed for spatial patterns.

To suppress noise, the gridded maps from Sections 3.4 and 3.5 are filtered using a local sliding 3×3 Gaussian window ($1.5° \times 30°$) with a sigma of five grid elements for the Gaussian weight kernels in both longitudinal and latitudinal directions. Furthermore, interpolation using global spherical splines is applied for representation of level variations within the grid elements.

4. Results

The south pole topography represented by the reference DTM from self-registering the reprocessed MOLA profiles is shown in Figure 1a. Before the analysis within local grid elements, the general trend of the seasonal snow/ice level against latitudes is studied by applying the proposed approach at different latitudinal annuli. Specifically, temporal level variations are obtained at seven different latitude bands of 2°, centered at 48°S, 62°S, 72°S, 80°S, 82°S, 84°S, and 86°S (Figure 2a). The precision of these results, as indicated from the scattering of the measurements, is found to be better than 10 cm. The peak-to-peak amplitudes of the variations gradually decrease from ∼1.7 m at 86° to ∼0.5 m at 62°S, and then to ∼0.3 m at 48°S. As the latter marks approximately the maximum extent of the SSPC, we consider ∼0.3 m as the accuracy of the obtained measurements for all annuli. Results from two previous studies, that is, Smith et al. (2001) at annulus 86.5°S and Aharonson et al. (2004) at annulus 86°S are also plotted for comparison. It is noteworthy that the peak-to-peak level variation of our result for annulus 86°S nearly doubles that of Smith et al. (2001), but is significantly lower than that of Aharonson et al. (2004). The off-season increase in southern summer and fall, which is present both in our results and in previous ones, is discussed in Section 5.1.

Further, the annulus analysis is extended to continuously cover the entire range of latitudes from 50° to 87°S with an interval of 2° in latitude. The total volume of the SSPC for each time step is then obtained by adding contributions from all different annuli (Figure 2b). Volume is computed by multiplying the measured level of snow/ice of each annulus by the area of each annulus, with Mars assumed as an ellipsoid with an equatorial radius of 3,396.19 km and a south polar radius of 3,379.21 km. For the small gap poleward of 87°S, it is assumed that the variations in level of snow and ice are identical to that acquired at the neighboring annulus 86°S. Volume contributions from latitudes equatorward of 50°S are considered negligible (Schmidt et al., 2010). After increasing during southern winter, the total volume of snow and ice generally decreases during late southern winter and spring as snow/ice sublimates and reduces to a minimum. The off-season increase during southern spring is discussed in Section 5.1. The total volume during southern summer and fall is erratic and not shown, which should be considered as an artifact, as discussed in Section 5.1. The peak volume is approximately 9.4×10^{12} m^3 in Martian Year 24 (MY24) and is 8.6×10^{12} m^3 in MY25. Meanwhile, the peak in MY24 is reached later by ∼15° in solar longitude (L_s) than observed in MY25.

A typical level variation time series for a grid element ([85.75°S, 86.25°S, 180°E, 190°E]) is illustrated in Figure 3. As we are interested in the relative level variations, the minimum is set to zero. The level of the SSPC maximizes at around L_s 165° to be ∼2 m, slightly lower than 2.5 m for the annulus 86°S from Aharonson et al. (2004). The peak level in MY25 is ∼0.3 m less than that in MY24. Movie S1 on the spatio-temporal variations in level of the SSPC is available as the supplementary material to this paper (see also Xiao, Stark, Schmidt, et al., 2021).

Map of the peak-to-peak level variations or the maximum snow/ice level of the SSPC is shown in Figure 1b. The associated precision, as measured by the scaled median absolute deviation, is normally better than 20 cm and below 10 cm poleward of 80°S (Figure S1 in Supporting Information S1). This map illustrates the spatial

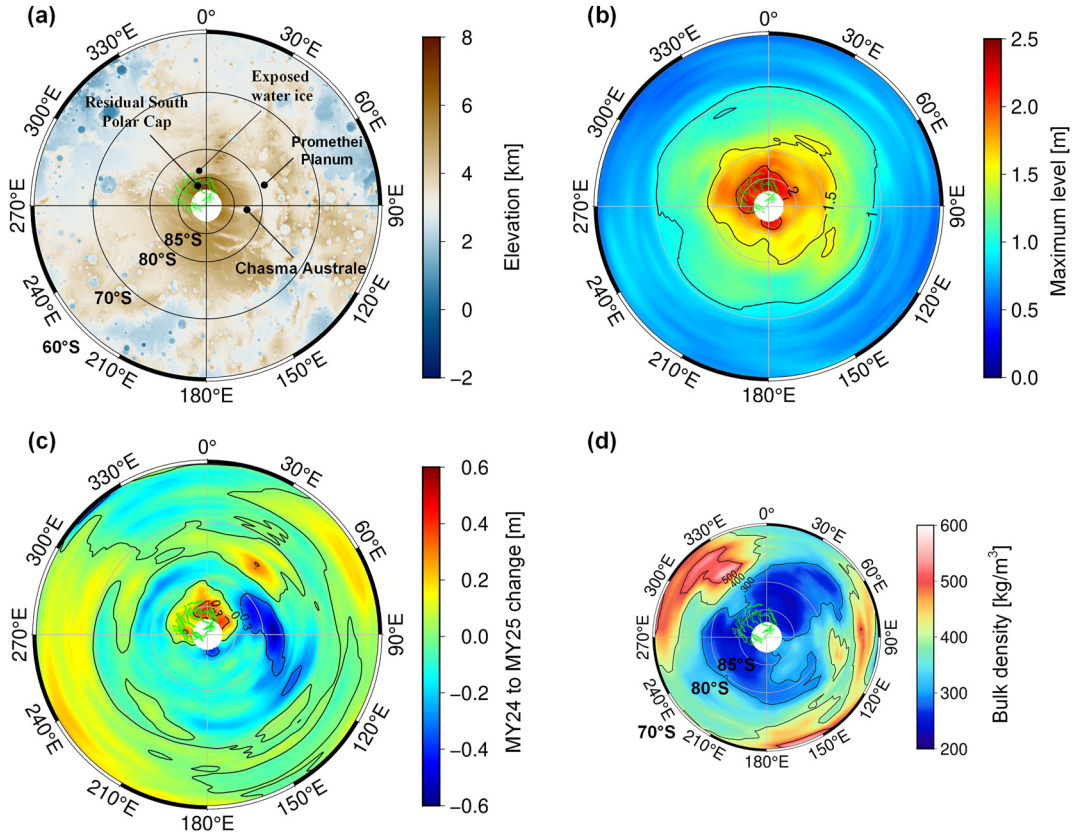

Figure 1. (a) Topography of the Martian south pole from the self-registered Mars Orbiter Laser Altimeter reference digital terrain model with respect to a Martian ellipsoid with an equatorial radius of 3,396.19 km and a mean polar radius of 3,376.20 km. (b) Maximum level. (c) Interannual peak level variation. Yellow and red colors mean there is higher snow/ice level in M25 than in MY24. The adopted projection is polar stereographic centered at the south pole. (d) Bulk density of the Seasonal South Polar Cap during its recession. Warmer tone denotes higher bulk density, which is equivalent to smaller porosity. Map format is the same as from (a) to (c) except that the map coverage ranges from 70° to 87°S. Boundary of the Residual South Polar Cap from Skinner Jr et al. (2006) is marked in green. For (b) to (d), contours are also added.

distribution of the maximum seasonal CO_2 level, in particular its non-axisymmetric pattern within annuli. The largest magnitudes up to ~2.5 m are located at the Residual South Polar Cap and regions poleward of 85°S, which can be related to the higher albedo and lower solar elevation angles (resulting in higher condensation and lower sublimation rates) compared to the surroundings (Gary-Bicas et al., 2020). Large magnitudes also occur on the exposed water ice patch (from 82° to 84°S and 315° to 5°E) along the northern margins of the Residual South Polar Cap (Titus et al., 2003), which supports deposition and retention of the deposits (Calvin et al., 2017). In addition, no dichotomy is observed in the maximum level variations at the cryptic and non-cryptic regions.

The statistics of the maximum snow/ice level, that is, mean, maximum, and standard deviation, are examined in each 0.5° latitudinal annulus (Figure 4). ward of 67.5°S, the mean of the maximum snow/ice level appears to increase almost linearly with latitude at an average rate of ~5.5 cm/degree. The mean level within the edge of the Residual South Polar Cap (poleward of ~84°S) steadily increases before it stabilizes at ~2 m, which is due to the asymmetric distribution of the Residual South Polar Cap around the south pole. The variability of the level within each annulus is expressed by the standard deviation, which ranges from 0.1 to 0.25 m. In addition, we show the average solar longitude corresponding to the maximum level against latitude at a step of 0.5° (green crosses in Figure 4). We can see that the level begins to decline at 60°S after peaking at L_s ~150° right after the middle southern winter. However, the accumulation lasts longer at higher latitudes, and the SSPC over the Residual South Polar Cap only begins to thin at L_s ~170° in the late southern winter. These time stamps also correspond well with the curves obtained at various annuli (Figure 2).

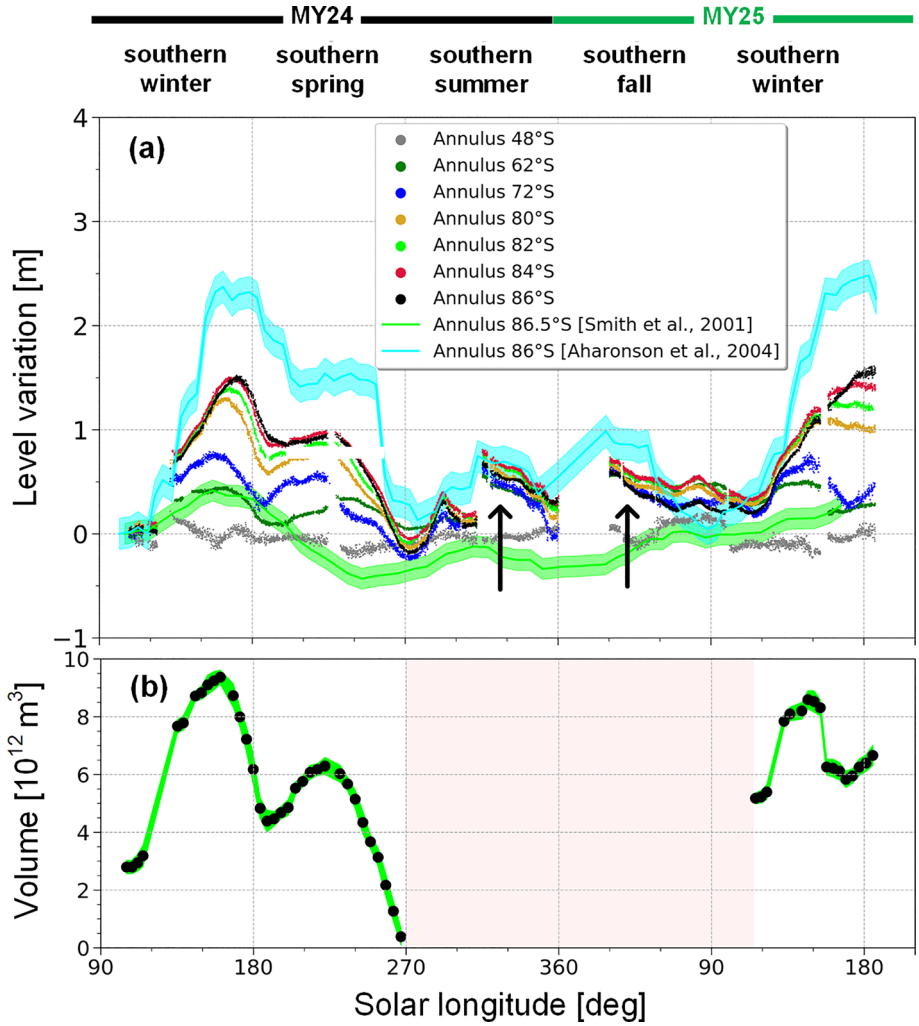

Figure 2. (a) Temporal level variations at selected annuli. Contrarily to that observed in southern winter and spring, the arrows indicate artifacts in the southern summer and fall since the latitude dependence is not smoothly decreasing. Results from two previous studies are shown for comparison. (b) Total volume deduced from the temporal level variations in the annuli poleward of 50°S. Red shade denotes the time period that features data considered to be in error (see text for details).

By comparison of the interannual peak level of snow and ice in MY24 and MY25 (Figures 1c and S2 in Supporting Information S1), we can see that the peak level at MY25 is normally ~0.5 m higher than that at MY24 over the Residual South Polar Cap, indicating either increased deposition in MY25 or thickened Residual South Polar Cap in MY24. Exceptions are the lower peak level in MY25 than in MY24, which mainly cluster in topographic lows of Chasma Australe and the attached Promethei Planum (refer to Figure for locations).

A typical temporal mass change rate for the grid element of (85.75°S, 86.25°S, 180°E, 190°E), together with the associated temporal level variation is shown in Figure 5. While the level of snow and ice culminates at around L_s 160° and begins to generally decline thereafter, the mass predicted by the energy balance model still accumulates until around L_s 200°, but with diminishing rate during southern spring. The aforementioned desynchrony is noted to be ubiquitous at all grid elements, which could be that the height loss due to densification begins to outweigh the height accumulation at the end of southern winter. The off-season increase in southern summer observed by MOLA is considered to be an artifact, as discussed in Section 5.1, so the comparison to the mass change rate is meaningless. Here, we derive the average bulk density of the SSPC during the recession phase, defined here as the period of level declination from the maximum at the middle-to-late southern winter all the way to 0 at the end of southern spring or beginning of southern summer. The bulk density is obtained from dividing the corresponding net sublimated mass (sublimated minus condensed) per unit area integrated at the recession

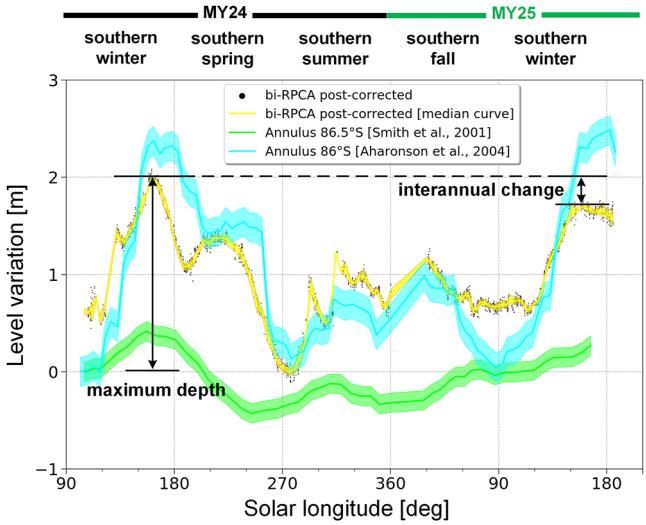

Figure 3. Level variation time series for a selected grid element along 86°S ([85.75°S, 86.25°S, 180°E, 190°E]). Yellow shade denotes the precision of the median-binned temporal curve measured by the scaled median absolute deviation. Two key statistical characteristics for interpretation are marked.

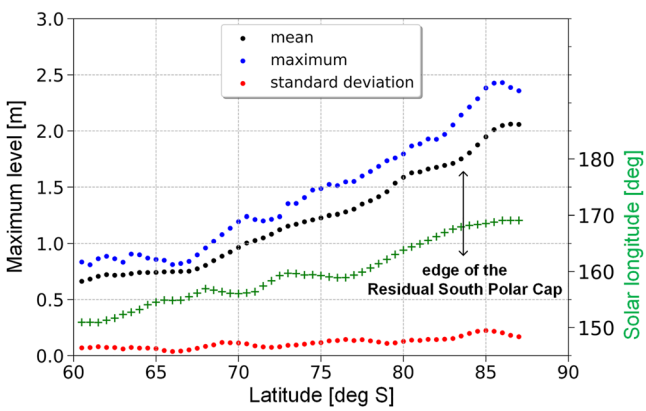

Figure 4. Statistics of the seasonal CO_2 polar cap maximum level as a function of latitude. Green crosses show the average solar longitude when the maximum level is reached with respect to latitude.

phase, defined here as when the level is declining, by the maximum level at MY24 (as marked in Figure 5). The maximum level decreases with latitudes and becomes less than ~1 m equatorward of 70°S (Figure 1b). In this case, its variation due to the associated measurement error can be magnified in the aforementioned division process and leads to noisy and unreliable bulk density measurements at individual grid elements. Meanwhile, as the MOLA profiles become sparser toward lower latitudes, the measurement error associated with the maximum level also increases and further contaminates the bulk density measurements. Thus, we spatially restrict our analysis to regions poleward of 70°S. The spatial distribution of the bulk density of the SSPC during recession is shown in Figure 1d. Patches at the Residual South Polar Cap and its surrounding regions feature the lowest values in the range of ~300 to ~600 kg/m^3, some of which are even lower than the threshold of 420 kg/m^3 for snow (74% porosity; Mount & Titus, 2015). Meanwhile, regions within 70° to 80°S feature higher bulk densities that can vary from ~600 kg/m^3 to up to 1,500 kg/m^3, some of which are even higher than the threshold of slab ice (1,190 kg/m^3 with 26% porosity; Mount & Titus, 2015). We can also see that poleward of 75°S the bulk density at the cryptic region is generally higher than that at the non-cryptic region, but it is spatially inhomogeneous with a large range of ~200 to ~500 kg/m^3).

5. Discussions

5.1. Off-Season Increase and Decrease

The off-season increase (within L_s 180°–230°) of snow and ice of up to 1 m in southern springtime (Figures 6 and S3 in Supporting Information S1), particularly pervasive over the south pole, remains unexplained. This is also reflected as the spring increase of ~2×10^{12} m^3 in the volume evolution as shown in Figure 2b. The level variation time series at 86.5°S from Aharonson et al. (2004) also exhibits slight springtime increase but it is within the uncertainty bars. Spring increase commences earlier and its magnitude becomes larger at annuli with lower latitudes, for example, ~0.1 m at annulus 86°S and ~0.3 m at annulus 72°S (Figure 2a). As the surface area of each 2° annulus increases with lower latitudes, the volume increase during springtime is dominated by those signals obtained at lower latitudes. Interestingly, Pommerol et al. (2011) observed that both the albedo and CO_2 spectral band depth around the south pole present an unexpected increase from L_s ~ 200° to ~250° during the southern spring. They attributed these to the predominance of surficial sublimation of the CO_2 ice layer which releases some of the water ice and dust particles that are then blown away by the winds. This theory is also in agreement with our observations which would lead to an increase of surface reflectance and CO_2 spectral band depth. Indeed, it is frequently observed in satellite images that dark deposits can entirely disappear during mid-spring below a brighter and bluer veil before they re-appear almost intact later in spring (e.g., Pommerol et al., 2011). Andrieu et al. (2018) applied Bayesian inversion techniques involving a radiative transfer model to constrain the changing level of the SSPC at Richardson Crater (72°S, 180°W), where off-season spring increase of ~0.1 m is found at three out of four of their test sites. They attributed the measured increase in thickness to dust migration within the ice, producing an optically thick layer of dust burrowing downwards. In fact, Langevin et al. (2006) argued that granular CO_2 ice could be deposited on top of the seasonal ice layer by the cold-jetting process itself via adiabatic cooling of the gas jets. However, the thickness of these fine-grained deposits is speculated to be just on mm-level. Note that MOLA pulses are often found to be saturated when the instrument is operating over bright polar areas in the early to-mid southern spring (Text S1 in Supporting Information S1). Thus, the range walk corrections, typically applied to the data, may be biased, which then could translate into the observed transient springtime increase. A solution

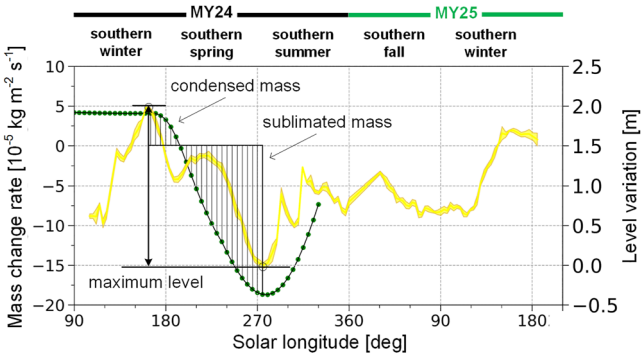

Figure 5. Temporal mass change rate at the grid element of (85.75°S, 86.25°S, 180°E, 190°E). The corresponding temporal level variation is also plotted, same as that in Figure 3. Maximum level of the Seasonal South Polar Cap during MY24, and the net sublimated mass, that is, sublimated minus condensed, per unit area integrated when the level in on the decline, are marked.

would be to simulate the full waveform of the saturated pulses (e.g., Budge et al., 2006; Jacob et al., 2008) and re-estimate the range walk corrections, by taking footprint-scale topography measured from high-resolution DTMs such as that from High Resolution Imaging Science Experiment (HiRISE; McEwen et al., 2007), Color and Stereo Surface Imaging System (CaSSIS; Thomas et al., 2017), and Context Camera (CTX; Malin et al., 2007) images. As preliminary treatment of the simulation implementation, we would need to precisely align the MOLA footprints and the high-resolution DTMs by co-registration techniques (Xiao, Stark, Steinbrügge, et al., 2022). Meanwhile, the idea that the MOLA laser pulses at 1,064 nm may partially penetrate the translucent slab ice during southern spring is ruled out (Text S2 in Supporting Information S1).

The observed abrupt increase and subsequent rapid loss of snow/ice in southern summer (L_s 270°–360°; Figure 2a), have been identified previously, as indicated by the relatively large amplitudes of the semi-annual sinusoidal term in Figure 7c in Aharonson et al. (2004). Interestingly, the off-season summer increase is spatially confined to regions poleward of ~60°S. Unlike the curves during the southern winter and spring which gradually decrease in magnitudes in annuli at lower latitudes, those during southern summer stay nearly the same (Figure 2a). The shadowing by topography is local and the squalls can be temporary, which runs contrary to the temporally and spatially extensive presence of these summer and fall biases. Thus, these two factors can be ruled out as possible causes. Meanwhile, it is observed by MGS Thermal Emission Spectrometer (TES) that the annuli from 50° to 70°S are free of seasonal ice in the southern summers from MY23 to MY31 (Piqueux et al., 2015). Evidence for surface ice is also lacking in Mars Orbiter Camera (MOC) images acquired at MY24 and MY25 (James et al., 2007; Wang & Ingersoll, 2002). In addition, the off-season summer increase has not been verified yet using other formats of measurements, such as the Neutron Spectrometer, GCMs, and energy balance model (Feldman et al., 2003; Prettyman et al., 2009; Schmidt et al., 2010; Smith et al., 2009). To conclude, these summer decrease and increase observed by MOLA are considered as artifacts. As for the level decrease and increase in southern fall, it bears significant similarities to that in southern summer. Thus, there are also considered artifacts for the similar arguments.

The summer and fall curves are insensitive to different latitudes, indicating them to be the results of some systematic temporal bias. In contrast, the level oscillations during southern winter and spring can gradually and orderly decrease from ~1.8 m at 86° to nearly 0 at 48°S, which is also consistent with the observation that the lowest latitude SSPC can extend to is roughly 50°S (Piqueux et al., 2015). Time stamps when the level maximize are also orderly shifting from mid-winter at low latitudes to late-winter at high latitudes (Figures 2a and 4), which is in accordance with the gradual migration of the sublimation from the edge of the SSPC to the inner-most areas. Thus, we believe the biases responsible for the observed southern summer and fall artifacts do not act on the seasonal signal during in southern winter and spring.

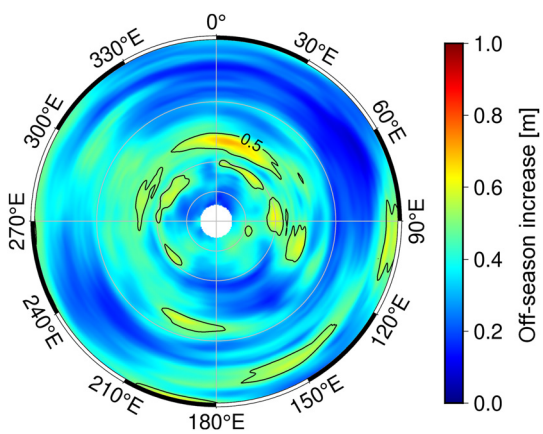

Figure 6. Off-season increase during southern spring examined within L_s 180°–230°. Map format is the same as in Figures 1a–1c.

5.2. Implications From the Measured Bulk Density Map

The lowest bulk density values cluster at the Residual South Polar Cap and its surroundings. There exists a general increase of the bulk density toward lower latitudes. These could be explained by higher concentration of CO_2 clouds, and hence snowfall, toward the Residual South Polar Cap and its surroundings (Cornwall & Titus, 2010; Gary-Bicas et al., 2020; Hayne et al., 2012). The phenomenon of atmospheric precipitation dominating in the western hemisphere may be due to the distinct climate regimes caused by the enormous Hellas and Argyre impact basins (Colaprete et al., 2005; Giuranna et al., 2008).

By comparing the mass of the SSPC from time-variable gravity measurements assuming a linear distribution of the surface mass density (Karatekin

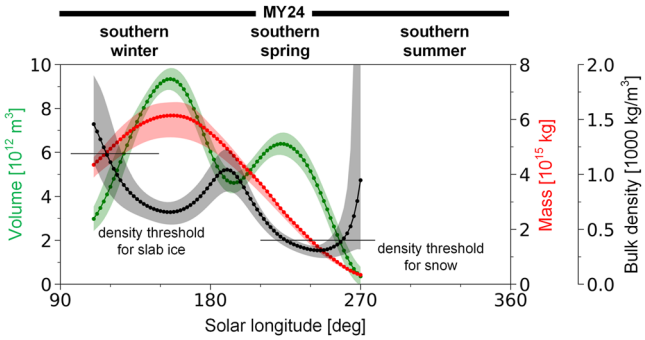

Figure 7. Fitted curve of the volume measurements in Figure 2b (green line), and the 95% confidence bounds (green shade). Also shown are the mass of the Seasonal South Polar Cap during southern winter and spring (red line and shade), and the resultant evolution of its bulk density (black line and shade). The bulk density thresholds for slab ice (1,190 kg/m^3) and snow (420 kg/m^3) are marked for reference.

et al., 2006), and the corresponding volume (Figure 2b), we can also look into the evolution of the bulk density of the SSPC. We fit the volume time series using the Gaussian Process regression in which a radial basis function kernel is adopted. The sigma added to the diagonal of the kernel matrix is assigned as two folds of the scaled median absolute deviation associated with each volume measurement. Volume measurements are then sampled from the fitted curve with an interval of 2° in solar longitude from L_s 110°–270°. The bulk density is obtained from dividing the mass of the SSPC by the corresponding volume measurement (black line in Figure 7). To estimate the uncertainties of the derived bulk densities, we also evaluate the lower and upper bounds of the mass measurements from Karatekin et al. (2006) against that of the volume measurements taken as the 95% confidence interval from the Gaussian Process fitting. Lower and upper bounds from Karatekin et al. (2006) are taken as model outputs assuming the poles as point masses and a constant surface mass density, respectively. The bounds of the mass and volume measurements, and the resultant bulk densities are represented by the corresponding shades in Figure 7. We can see that the bulk density actually decreases at the beginning-to-late wintertime from an initially high value of ∼1,450 kg/m^3, which is even much higher than the threshold for slab ice (1,190 kg/m^3). Then, it reaches a local minima when its volume maximizes (∼660 kg/m^3), which is followed by an increasing period. However, the transient spring accumulation, which could not be confirmed at current status (Section 5.1), cutoff the upward trend and leads it to a global minima of ∼300 kg/m^3. But, right after reaching the global minima, we can observe that it increases again to ∼950 kg/m^3 at the end of southern spring before the SSPC completely sublimates away.

The bulk density decrease during beginning-to-late southern winter (Figure 7) is in contrast to the normal assumption that it should continuously increase throughout fall, winter, and spring (e.g., Matsuo & Heki, 2009). It is likely that, initially the direct condensation dominates during the southern fall and early southern winter, then as the temperature continues to drop, snowfall gradually prevails. At accumulation phase during the fall and winter, starting with direct condensation has also been suggested by laboratory experiments (Grisolle, 2013). Some CO_2 ice experiments and observations also suggest that the density decrease trend could be due to fracturation (e.g., Grisolle, 2013; Mount & Titus, 2015). The bulk density of the SSPC when its volume maximizes is ∼660 kg/m^3, which actually corresponds to a local minima. Subsequently, there exists an upward period that could be attributed to compaction mechanisms such as annealing and re-crystallization (Eluszkiewicz et al., 2005; Matsuo & Heki, 2009). The resultant slab ice can undergo a self-cleaning process in which dust grains burrow downward or released through the upper surface, to become translucent and enable sunlight to reach the substrate, which is the key prerequisite for the cold-jetting mechanism at the cryptic region (Kieffer et al., 2006).

It is worthy to note that by the time the bulk density of the SSPC falls below 1,190 kg/m^3 during the southern winter, ∼4.8 × 10^{15} kg (or ∼80% of a total of ∼6 × 10^{15} kg) has already been accumulated to the surface (Figure 7). Thus, snowfall is largely limited to the Residual South Polar Cap and its surroundings as aforementioned, and overall it just constitutes of less than ∼20% of the total annual deposition. The deduced proportion is largely in agreement with the statement that snowfall constitutes only 3%–20% of the seasonal CO_2 deposits in latitudes between 70° and 90°S (Hayne et al., 2014).

6. Conclusion

Based upon methods we developed previously (Xiao, Stark, Steinbrügge, et al., 2022), we retrieve variations in the snow/ice level of the Mars' SSPC from MOLA data by applying a local co-registration strategy complemented with a post-correction procedure based on pseudo cross-overs. The temporal level variation is obtained for each grid element of 0.5° in latitude and 10° in longitude. The maximum snow/ice level in the range of 2–2.5 m are found over the Residual South Polar Cap. Peak level at the Residual South Polar Cap in MY25 are normally ∼0.5 m higher than those in MY24. In addition, by applying the methods to different annuli, we find the peak volume is approximately 9.4 × 10^{12} m^3 in MY24 and 0.8 × 10^{12} m^3 less in MY25. Furthermore, we derive the bulk density, for the first time as map, of the SSPC during its recession by combining our data with corresponding

modeled mass change rates from surface's energy balance. Residual South Polar Cap and its surrounding regions feature lowest values in the range of ~300 to ~600 kg/m^3. These relatively low bulk densities there as compared to elsewhere is likely due to much more concentrated atmospheric precipitation. However, overall snowfall just constitutes of less than ~20% of the total mass of the SSPC. Direct condensation dominates during southern fall and early southern winter, and the bulk density of the SSPC actually decreases due to snowfall until its volume maximizes. Meanwhile, a time shift between the maximum level of the SSPC following ~40° in solar longitude later by the maximum mass of the SSPC is identified and proposed to be linked to the densification of the deposits, most probably by metamorphism.

This study sheds light on both the temporal and spatial level evolution of the SSPC, which stand as important constraints on future Martian climate and volatile models. In addition, our results can be combined with laboratory modeling to gain insights into the cold-jetting mechanism which is related to the thickness and state of the SSPC. As for the next step, we will do the same analysis to the Seasonal North Polar Cap (SNPC). These results will be analyzed against that of the SSPC to reveal different behaviors of the two seasonal polar caps. Meanwhile, total CO_2 budget evolution of the atmosphere-surface exchange can be obtained by analyzing the SSPC and SNPC as a whole. We will also apply the approach of Andrieu et al. (2018) to the entire SSPC to examine its level variations during the sublimation phase. Simultaneously, we will try the SHAllow RADar (SHARAD) radar altimetry (Seu et al., 2007; Steinbrügge et al., 2021) to derive long-term level variations of the seasonal polar caps of Mars. These independent results can also be used to cross-validate the off-season increase and decrease as measured by the MOLA data set.

Conflict of Interest

The authors declare no conflicts of interest relevant to this study.

Data Availability Statement

The MOLA PEDR data set (Version L) is available from the Planetary Data System (PDS) Geosciences Node at https://pds-geosciences.wustl.edu/missions/mgs/pedr.html (Smith et al., 2003). While the MGS trajectory and attitude kernels can be obtained from NASA NAIF at https://naif.jpl.nasa.gov/pub/naif/pds/data/mgs-m-spice-6-v1.0/mgsp_1000/data/ (Acton, 1996). The generated level variation time series in each grid element and various map products are published under https://doi.org/10.17632/z59b9nd6s9.2 (Xiao, Stark, Steinbrügge, et al., 2021). The mass change rate measurements used for deriving the bulk density of the snow/ice are published under https://doi.org/10.14768/8cba4407-d6a0-4d16-aeaf-d0ebfd2b480a (Schmidt, 2022).

Acknowledgments
The authors would like to thank N. Wagner (Baylor Univ.), A. Pommerol (Univ. Bern), and Y. Cheng (Tongji Univ.) for helpful discussions. H. Xiao thanks the China Scholarship Council (CSC) for financial support of his Ph.D. study in Germany. H. Xiao was also supported by a scholarship from the Deutsche Forschungsgemeinschaft (DFG) Grant SFB-TRR 170. Part of this research was carried out within the framework of the DLR BigData Querschnittsplattform. F. Schmidt acknowledges support from the "Institut National des Sciences de l'Univers" (INSU), the "Centre National de la Recherche Scientifique" (CNRS), and "Centre National d'Etudes Spatiales" (CNES) through the "Programme National de Planétologie." We thank O. Aharonson (PSI & Weizmann Inst.), T. N. Titus (USGS), and an anonymous reviewer for a constructive review which helped to improve this contribution. We also acknowledge the MOLA and MGS teams for providing the great product that enabled this research. Open Access funding enabled and organized by Projekt DEAL.

References

Acton, C. H. J. (1996). Ancillary data services of NASA's Navigation and Ancillary Information Facility. *Planetary and Space Science*, *44*(1), 65–70. https://doi.org/10.1016/0032-0633(95)00107-7

Aharonson, O., Zuber, M. T., Smith, D. E., Neumann, G. A., Feldman, W. C., & Prettyman, T. H. (2004). Depth, distribution, and density of CO_2 deposition on Mars. *Journal of Geophysical Research*, *109*(E5), E05004. https://doi.org/10.1029/2003JE002223

Andrieu, F., Schmidt, F., Douté, S., & Chassefière, E. (2018). Ice state evolution during spring in Richardson crater, Mars. *Icarus*, *315*, 158–173. https://doi.org/10.1016/j.icarus.2018.06.019

Archinal, B., Acton, C., A'Hearn, M., Conrad, A., Consolmagno, G., Duxbury, T., et al. (2018). Report of the IAU working group on cartographic coordinates and rotational elements: 2015. *Celestial Mechanics and Dynamical Astronomy*, *130*(3), 22. https://doi.org/10.1007/s10569-017-9805-5

Barker, M., Mazarico, E., Neumann, G., Zuber, M., Haruyama, J., & Smith, D. (2016). A new lunar digital elevation model from the lunar orbiter laser altimeter and SELENE terrain camera. *Icarus*, *273*, 346–355. https://doi.org/10.1016/j.icarus.2015.07.039

Bibring, J. P., Soufflot, A., Berthé, M., Langevin, Y., Gondet, B., Drossart, P., et al. (2004). OMEGA: Observatoire pour la Minéralogie, l'Eau, les Glaces et l'Activité. In A. Wilson & A. Chicarro (Eds.). *Mars Express: The scientific payload*. (Vol. 1240, pp. 37–49).

Budge, S., Leishman, B., & Pack, R. (2006). Simulation and modeling of return waveforms from a ladar beam footprint in USU LadarSIM. *Laser Radar Technology and Applications XI*, *6214*. https://doi.org/10.1117/12.666404

Calvin, W., Cantor, B., & James, P. (2017). Interannual and seasonal changes in the South Seasonal Polar Cap of Mars: Observations from MY 28-31 using MARCI. *Icarus*, *292*, 144–153. https://doi.org/10.1016/j.icarus.2017.01.010

Colaprete, A., Barnes, J. R., Haberle, R. M., Hollingsworth, J. L., Kieffer, H. H., & Titus, T. N. (2005). Albedo of the south pole on Mars determined by topographic forcing of atmosphere dynamics. *Nature*, *435*(7039), 184–188. https://doi.org/10.1038/nature03561

Cornwall, C., & Titus, T. N. (2010). A comparison of Martian north and south polar cold spots and the long-term effects of the 2001 global dust storm. *Journal of Geophysical Research*, *115*(E6), E06011. https://doi.org/10.1029/2009JE003514

Diniega, S., Bramson, A. M., Buratti, B., Buhler, P., Burr, D. M., Chojnacki, M., et al. (2021). Modern Mars' geomorphological activity, driven by wind, frost, and gravity. *Geomorphology*, *380*, 107627. https://doi.org/10.1016/j.geomorph.2021.107627

Eluszkiewicz, J., Moncet, J.-L., Titus, T. N., & Hansen, G. B. (2005). A microphysically-based approach to modeling emissivity and albedo of the Martian seasonal caps. *Icarus*, *174*(2), 524–534. https://doi.org/10.1016/j.icarus.2004.05.025

Feldman, W., Prettyman, T., Boynton, W. V., Murphy, J., Squyres, S., Karunatillake, S., & Kerry, K. (2003). CO_2 frost cap thickness on Mars during northern winter and spring. *Journal of Geophysical Research*, *108*(E9), 5103. https://doi.org/10.1029/2003JE002101

Gary-Bicas, C., Hayne, P., Horvath, T., Heavens, N., Kass, D., Kleinböhl, A., et al. (2020). Asymmetries in snowfall, emissivity, and albedo of Mars' seasonal polar caps: Mars Climate Sounder observations. *Journal of Geophysical Research: Planets*, *125*(5), e2019JE006150. https://doi.org/10.1029/2019JE006150

Giuranna, M., Grassi, D., Formisano, V., Montabone, L., Forget, F., & Zasova, L. (2008). PFS/MEX observations of the condensing CO_2 south polar cap of Mars. *Icarus*, *197*(2), 386–402. https://doi.org/10.1016/j.icarus.2008.05.019

Grisolle, F. (2013). *Seasonal condensates on Mars: Experimental study of formation and metamorphism of CO_2 ices* (Ph.D. thesis, Université de Grenoble). Retrieved from https://tel.archives-ouvertes.fr/tel-01010519

Hansen, C., Thomas, N., Portyankina, G., McEwen, A., Becker, T., Byrne, S., et al. (2010). HiRISE observations of gas sublimation-driven activity in Mars' southern polar regions: I. Erosion of the surface. *Icarus*, *205*(1), 283–295. https://doi.org/10.1016/j.icarus.2009.07.021

Hao, J., Michael, G., Adeli, S., & Jaumann, R. (2019). Araneiform terrain formation in Angustus Labyrinthus, Mars. *Icarus*, *317*, 479–490. https://doi.org/10.1016/j.icarus.2018.07.026

Hao, J., Michael, G., Adeli, S., Jaumann, R., Portyankina, G., Hauber, E., et al. (2020). Variability of spider spatial configuration at the Martian south pole. *Planetary and Space Science*, *185*, 104848. https://doi.org/10.1016/j.pss.2020.104848

Hayne, P. O., Paige, D. A., Heavens, N. G., & the Mars Climate Sounder Science Team. (2014). The role of snowfall in forming the seasonal ice caps of Mars: Models and constraints from the Mars Climate Sounder. *Icarus*, *231*, 122–130. https://doi.org/10.1016/j.icarus.2013.10.020

Hayne, P. O., Paige, D. A., Schofield, J. T., Kass, D. M., Kleinböhl, A., Heavens, N. G., & McCleese, D. J. (2012). Carbon dioxide snow clouds on Mars: South polar winter observations by the Mars Climate Sounder. *Journal of Geophysical Research*, *117*(E8). 2011JE004040. https://doi.org/10.1029/2011JE004040

Jacob, D., Gatt, P., & Nichols, T. (2008). Overview of LMCT's advanced ladar signal simulator (ALASS). *Laser Radar Technology and Applications XIII*, *6950*. https://doi.org/10.1117/12.798024

James, P. B., Thomas, P. C., Wolff, M. J., & Bonev, B. P. (2007). MOC observations of four Mars year variations in the south polar residual cap of Mars. *Icarus*, *192*(2), 318–326. https://doi.org/10.1016/j.icarus.2007.07.014

Jian, J.-J., & Ip, W.-H. (2009). Seasonal patterns of condensation and sublimation cycles in the cryptic and non-cryptic regions of the south pole. *Advances in Space Research*, *43*(1), 138–142. https://doi.org/10.1016/j.asr.2008.05.002

Karatekin, Ö., Van Hoolst, T., & Dehant, V. (2006). Martian global-scale CO_2 exchange from time-variable gravity measurements. *Journal of Geophysical Research*, *111*(E6), E06003. https://doi.org/10.1029/2005JE002591

Kelly, N. J., Boynton, W. V., Kerry, K., Hamara, D., Janes, D., Reedy, R., et al. (2006). Seasonal polar carbon dioxide frost on Mars: CO_2 mass and columnar thickness distribution. *Journal of Geophysical Research*, *111*(E3), E03S07. https://doi.org/10.1029/2006JE002678

Kieffer, H. H. (2007). Cold jets in the Martian polar caps. *Journal of Geophysical Research*, *112*(E8), E08005. https://doi.org/10.1029/2006JE002816

Kieffer, H. H., Christensen, P. R., & Titus, T. N. (2006). CO_2 jets formed by sublimation beneath translucent slab ice in Mars' seasonal south polar ice cap. *Nature*, *442*(7104), 793–796. https://doi.org/10.1038/nature04945

Konopliv, A. S., Yoder, C. F., Standish, E. M., Yuan, D.-N., & Sjogren, W. L. (2006). A global solution for the Mars static and seasonal gravity, Mars orientation, Phobos and Deimos masses, and Mars ephemeris. *Icarus*, *182*(1), 23–50. https://doi.org/10.1016/j.icarus.2005.12.025

Langevin, Y., Douté, S., Vincendon, M., Poulet, F., Bibring, J.-P., Gondet, B., et al. (2006). No signature of clear CO_2 ice from the 'cryptic' regions in Mars' south seasonal polar cap. *Nature*, *442*(7104), 790–792. https://doi.org/10.1038/nature05012

Leighton, R. B., & Murray, B. C. (1966). Behavior of carbon dioxide and other volatiles on Mars. *Science*, *153*(3732), 136–144. https://doi.org/10.1126/science.153.3732.136

Leys, C., Ley, C., Klein, O., Bernard, P., & Licata, L. (2013). Detecting outliers: Do not use standard deviation around the mean, use absolute deviation around the median. *Journal of Experimental Social Psychology*, *49*(4), 764–766. https://doi.org/10.1016/j.jesp.2013.03.013

Litvak, M. L., Mitrofanov, I., Kozyrev, A., Sanin, A., Tretyakov, V., Boynton, W. V., et al. (2007). Long-term observations of southern winters on Mars: Estimations of column thickness, mass, and volume density of the seasonal CO_2 deposit from HEND/Odyssey data. *Journal of Geophysical Research*, *112*(E3), E03S13. https://doi.org/10.1029/2006JE002832

Malin, M. C., Bell, J. F., Cantor, B. A., Caplinger, M. A., Calvin, W. M., Clancy, R. T., et al. (2007). Context Camera investigation on board the Mars Reconnaissance Orbiter. *Journal of Geophysical Research*, *112*(E5), E05S04. https://doi.org/10.1029/2006JE002808

Matsuo, K., & Heki, K. (2009). Seasonal and inter-annual changes of volume density of Martian CO_2 snow from time-variable elevation and gravity. *Icarus*, *202*(1), 90–94. https://doi.org/10.1016/j.icarus.2009.02.023

Mazarico, E., Neumann, G., Rowlands, D., & Smith, D. (2010). Geodetic constraints from multi-beam laser altimeter crossovers. *Journal of Geodesy*, *84*(6), 343–354. https://doi.org/10.1007/s00190-010-0379-1

McEwen, A. S., Eliason, E. M., Bergstrom, J. W., Bridges, N. T., Hansen, C. J., Delamere, W. A., et al. (2007). Mars Reconnaissance Orbiter's High Resolution Imaging Science Experiment (HiRISE). *Journal of Geophysical Research*, *112*(E5), E05S02. https://doi.org/10.1029/2005JE002605

Mount, C. P., & Titus, T. N. (2015). Evolution of Mars' northern polar seasonal CO_2 deposits: Variations in surface brightness and bulk density. *Journal of Geophysical Research: Planets*, *120*(7), 1252–1266. https://doi.org/10.1002/2014JE004706

Piqueux, S., & Christensen, P. R. (2008). North and south subice gas flow and venting of the seasonal caps of Mars: A major geomorphological agent. *Journal of Geophysical Research*, *113*(E6), E06005. https://doi.org/10.1029/2007JE003009

Piqueux, S., Kleinböhl, A., Hayne, P. O., Kass, D. M., Schofield, J. T., & McCleese, D. J. (2015). Variability of the Martian seasonal CO_2 cap extent over eight Mars Years. *Icarus*, *251*, 164–180. https://doi.org/10.1016/j.icarus.2014.10.045

Pommerol, A., Portyankina, G., Thomas, N., Aye, K.-M., Hansen, C., Vincendon, M., & Langevin, Y. (2011). Evolution of south seasonal cap during Martian spring: Insights from high-resolution observations by HiRISE and CRISM on Mars Reconnaissance Orbiter. *Journal of Geophysical Research*, *116*(E8), E08007. https://doi.org/10.1029/2010JE003790

Portyankina, G., Hansen, C. J., & Aye, K.-M. (2017). Present-day erosion of Martian polar terrain by the seasonal CO_2 jets. *Icarus*, *282*, 93–103. https://doi.org/10.1016/j.icarus.2016.09.007

Prettyman, T. H., Feldman, W. C., & Titus, T. N. (2009). Characterization of Mars' seasonal caps using neutron spectroscopy. *Journal of Geophysical Research*, *114*(E8), 2008JE003275. https://doi.org/10.1029/2008JE003275

Schmidt, F. (2022). D-frost potential daily CO_2 sublimation mass of the South polar cap of Mars. *IPSL Data Catalog*. https://doi.org/10.14768/8cba4407-d6a0-4d16-aeaf-d0ebfd2b480a

Schmidt, F., Douté, S., Schmitt, B., Vincendon, M., Bibring, J.-P., Langevin, Y., & the OMEGA Team. (2009). Albedo control of Seasonal South Polar Cap recession on Mars. *Icarus*, *200*(2), 374–394. https://doi.org/10.1016/j.icarus.2008.12.014

Schmidt, F., & Portyankina, G. (2018). The exotic processes driving ephemeral seasonal surface change on Mars. In *Dynamic Mars: Recent and current landscape evolution of the red planet* (pp. 157–186). Elsevier. https://doi.org/10.1016/B978-0-12-813018-6.00005-4

Schmidt, F., Schmitt, B., Douté, S., Forget, F., Jian, J.-J., Martin, P., et al. (2010). Sublimation of the Martian CO_2 Seasonal South Polar Cap. *Planetary and Space Science*, *58*(10), 1129–1138. https://doi.org/10.1016/j.pss.2010.03.018

Seu, R., Phillips, R. J., Biccari, D., Orosei, R., Masdea, A., Picardi, G., et al. (2007). SHARAD sounding radar on the Mars Reconnaissance Orbiter. *Journal of Geophysical Research*, *112*(E5), E05S05. https://doi.org/10.1029/2006JE002745

Skinner, J., Jr., Hare, T., & Tanaka, K. (2006). Digital renovation of the atlas of Mars 1: 15,000,000-scale global geologic series maps. In *37th Lunar and Planetary Science Conference* (p. 2331).

Smith, D. E., & Zuber, M. T. (2018). Depth, volume and density of Mars' seasonal polar caps. *European Planetary Science Congress*. EPSC2018–429.

Smith, D. E., Zuber, M. T., & Neumann, G. A. (2001). Seasonal variations of snow depth on Mars. *Science*, *294*(5549), 2141–2146. https://doi.org/10.1126/science.1066556

Smith, D. E., Zuber, M. T., Neumann, G. A., & Jester, P. (2003). Mars Global Surveyor Laser Altimeter Precision Experiment Data Record (PEDR). *NASA Planetary Data System*. Accessed on September 7, 2018. https://doi.org/10.17189/1519520

Smith, D. E., Zuber, M. T., Torrence, M. H., Dunn, P. J., Neumann, G. A., Lemoine, F. G., & Fricke, S. K. (2009). Time variations of Mars' gravitational field and seasonal changes in the masses of the polar ice caps. *Journal of Geophysical Research*, *114*(E5), E05002. https://doi.org/10.1029/2008JE003267

Stark, A., Oberst, J., Preusker, F., Peale, S. J., Margot, J.-L., Phillips, R. J., et al. (2015). First MESSENGER orbital observations of Mercury's librations. *Geophysical Research Letters*, *42*(19), 7881–7889. https://doi.org/10.1002/2015GL065152

Steinbrügge, G., Haynes, M. S., Schroeder, D. M., Scanlan, K. M., Stark, A., Young, D. A., et al. (2021). Altimetry measurements from planetary radar sounders and application to SHARAD on Mars. *IEEE Transactions on Geoscience and Remote Sensing*, *60*, 1–14. https://doi.org/10.1109/TGRS.2021.3134638

Steinbrügge, G., Stark, A., Hussmann, H., Sohl, F., & Oberst, J. (2015). Measuring tidal deformations by laser altimetry: A performance model for the Ganymede Laser Altimeter. *Planetary and Space Science*, *117*, 184–191. https://doi.org/10.1016/j.pss.2015.06.013

Thomas, N., Cremonese, G., Ziethe, R., Gerber, M., Brändli, M., Bruno, G., et al. (2017). The Colour and Stereo Surface Imaging System (CaSSIS) for the ExoMars Trace Gas Orbiter. *Space Science Reviews*, *212*(3), 1897–1944. https://doi.org/10.1007/s11214-017-0421-1

Titus, T. N., Kieffer, H. H., & Christensen, P. R. (2003). Exposed water ice discovered near the south pole of Mars. *Science*, *299*(5609), 1048–1051. https://doi.org/10.1126/science.1080497

Wagner, N., James, P., Ermakov, A., & Sori, M. (2022). Quantifying lithospheric deflection caused by seasonal mass transport from the Polar Layered Deposits on Mars. In *53rd Lunar and Planetary Science Conference* (p. 2352).

Wang, H., & Ingersoll, A. P. (2002). Martian clouds observed by Mars Global Surveyor Mars Orbiter Camera. *Journal of Geophysical Research*, *107*(E10), 8–1. https://doi.org/10.1029/2001JE001815

Xiao, H., Stark, A., Chen, H., & Oberst, J. (2022). Recomputation and updating of MOLA geolocation. *Remote Sensing*, *14*(9), 2201. https://doi.org/10.3390/rs14092201

Xiao, H., Stark, A., Schmidt, F., Hao, J., Steinbrügge, G., & Oberst, J. (2021). Spatio-temporal level variations of the Martian Seasonal South Polar Cap. *Mendeley Data*. https://doi.org/10.17632/z59b9nd6s9.2

Xiao, H., Stark, A., Steinbrügge, G., Hussmann, H., & Oberst, J. (2021). Processing of laser altimeter Time-of-Flight measurements to geodetic coordinates. *Journal of Geodesy*, *95*(2), 1–23. https://doi.org/10.1007/s00190-020-01467-4

Xiao, H., Stark, A., Steinbrügge, G., Thor, R., Schmidt, F., & Oberst, J. (2022). Prospects for mapping temporal height variations of the seasonal CO_2 snow/ice caps at the Martian poles by co-registration of MOLA Profiles. *Planetary and Space Science*, *214C*, 105446. https://doi.org/10.1016/j.pss.2022.105446

Zuber, M. T., Smith, D., Solomon, S., Muhleman, D., Head, J., Garvin, J., et al. (1992). The Mars Observer laser altimeter investigation. *Journal of Geophysical Research*, *97*(E5), 7781–7797. https://doi.org/10.1029/92JE00341

References From the Supporting Information

Abshire, J. B., Sun, X., & Afzal, R. S. (2000). Mars Orbiter Laser Altimeter: Receiver model and performance analysis. *Applied Optics*, *39*(15), 2449–2460. https://doi.org/10.1364/AO.39.002449

Chinnery, H. E., Hagermann, A., Kaufmann, E., & Lewis, S. R. (2020). The penetration of solar radiation into granular carbon dioxide and water ices of varying grain sizes on Mars. *Journal of Geophysical Research: Planets*, *125*(4), e2019JE006097. https://doi.org/10.1029/2019JE006097

Neumann, G. A., Abshire, J. B., Aharonson, O., Garvin, J. B., Sun, X., & Zuber, M. T. (2003). Mars Orbiter Laser Altimeter pulse width measurements and footprint-scale roughness. *Geophysical Research Letters*, *30*(11), 1561. https://doi.org/10.1029/2003GL017048

Neumann, G. A., Rowlands, D. D., Lemoine, F. G., Smith, D. E., & Zuber, M. T. (2001). Crossover analysis of Mars Orbiter Laser Altimeter data. *Journal of Geophysical Research*, *106*(E10), 23753–23768. https://doi.org/10.1029/2000JE001381